On the Interpretation of Coherent Marine Radar Backscatter From Surf Zone Waves

Michael Streßer, Jörg Seemann, Ruben Carrasco, Marius Cysewski, Jochen Horstmann, Burkard Baschek, and Grant Deane

***Abstract*— Observations of microwave backscatter from shoaling and breaking surface waves acquired with a shore-based, coherent-on-receive X-band marine radar are presented. The radar was located at the dune cliff of a sandy beach with two breaker bars. Waves were approximately shore-normal (inclination < 10°) during the study period. Consistent with other studies, the backscatter intensity from breaking waves is significantly increased (≈10 dB compared to nonbreaking) with Doppler velocities close to the wave phase velocity in shallow water. The strong backscatter from active breakers can cause a significant amount of signal artifacts due to the leakage of pulse energy into adjacent range cells, in particular behind the breaking crests. In the near range, the backscatter from the undisturbed surface and such pulse smearing artifacts appear as distinct peaks inside the Doppler spectra. Thus, the velocity of both sources of scatterering can be retrieved using a dedicated peak separation algorithm. In the far range (r > 500 m), the artifacts dominate the Doppler signal behind breaking wave crests. Therefore, when investigating the spatio-temporal evolution of breaking wave-induced Doppler velocities with marine radar, the analysis should be restricted to the wave crests and the well-illuminated front faces of the waves. The evolution of Doppler spectra tracked along the crest of an exemplary individual breaking wave is extracted during the steepening, active- and post-breaking stage.**

***Index Terms*— Doppler radar, marine radar, remote sensing, sea surface electromagnetic scattering, surface waves, wave breaking.**

I. Introduction

SHORE-BASED imaging Doppler radar has high potential to observe shoaling and breaking waves both in space and time. This capability is often required, but not available for studies of surf zone hydro- and morphodynamics. Breaking waves mainly drive surf zone circulation (e.g., [1]) and are therefore relevant for e.g., swimmer safety [2], loads on structures [3], and the mobilization and transport of sediments [4]. Measurements of surf zone waves are complicated because instruments located in energetic, breaking wave environments are easily misplaced or damaged [5]. Thus, deployment and maintenance costs are high and long-term observations are rare [6]. Furthermore, nearshore hydrodynamics are characterized by a high spatial and temporal variability. This complicates surf zone observations using *in situ* sensors (e.g., acoustic sensors, pressure transducers, or wire gauges), in particular, for long-term monitoring.

Instead, shore-based remote sensing instruments provide observations in space and time and can be efficiently operated over longer periods. Besides widely used passive optical sensors, such as visible light or infrared cameras (see [7] for a review), imaging marine radar is an active remote sensing technique. Marine radar can be used to infer bathymetry [8]–[12], currents [13], [15], [16], or both simultaneously [14], [17], as well as directional wave spectra [18] and surface winds [19]–[21]. Marine radars, which are usually used for nautical navigation, have the advantage of being relatively inexpensive and easy to install and maintain. In contrast to camera-based methods, radar can be operated day and night and during foggy conditions. Spatial coverage is usually larger and geo-referencing of the imagery is relatively easy.

Imaging radars often operate at grazing incidence angles to achieve the desired range coverage. Compared to nadir looking radar wave gauges, which measure the distance to the surface, i.e., the strongest return signal, the retrieval of the vertical elevation of the ocean surface at grazing incidence is not trivial. The development of methods to directly invert marine radar images to surface elevation is the subject of past and current research [22]–[27]. However, a deterministic "wave-by-wave" validation of radar-based surface inversions has not been realized yet.

In addition to the backscatter intensity, coherent radar systems are able to measure the Doppler shift of the electromagnetic waves caused by moving targets at the water surface. This offers high potential for wave measurements (e.g., [28]–[32]) and for studying wave breaking [33]–[36]. However, there is not much literature available on coherent radar backscatter from shoaling and breaking nearshore waves. Important insight into the scattering dynamics (which are briefly summarized in Section II) was gained from scatterometer data [37]–[39]. However, only very few authors have used imaging coherent radar inside, or in direct vicinity of, the surf zone. McGregor *et al.* [29] used a frequency modulated continuous wave (FMCW) radar and were able to derive bathymetry and wave energy from their data. The elevation of their radar was relatively high (70 m) and hence

Manuscript received April 6, 2021; revised July 5, 2021; accepted August 2, 2021. Date of publication August 19, 2021; date of current version January 21, 2022. This work was supported by the Polar Regions and Coasts in the Changing Earth System (PACES II) Program of the Helmholtz Association. *(Corresponding authors: Michael Streßer; Jochen Horstmann.)*

Michael Streßer, Jörg Seemann, Ruben Carrasco, Marius Cysewski, Jochen Horstmann, and Burkard Baschek are with the Institute of Coastal Ocean Dynamics, Helmholtz-Zentrum Hereon, 21502 Geesthacht, Germany (e-mail: michael.stresser@hereon.de; jochen.horstmann@hereon.de).

Grant Deane is with the Marine Physical Laboratory, Scripps Institution of Oceanography, UC San Diego, La Jolla, CA 92093 USA.

Digital Object Identifier 10.1109/TGRS.2021.3103417

grazing angles were above 8° throughout the whole measurement area, spanning over ≈600 m. At these grazing angles, the backscatter from the ocean surface is considered to be reasonably described by Bragg scattering and composite-surface theory (CST, cf. Section II). McGregor *et al.* [29] also found that the radar-derived energy of breaking waves atop a sand bar is significantly overestimated. This is because horizontal surface velocities are significantly increased during breaking and thus also the variance of the radar measured Doppler velocity, which they used to infer wave energy. At much lower grazing angles of <2°, high correlations were reported between Doppler velocities observed with the focused phased array imaging radar (FOPAIR) and bore propagation speeds derived from particle imaging velocimetry (PIV) [40] as well as acoustic Doppler velocimeter (ADV) data [41]. However, Farquharson *et al.* [41] highlight that Doppler velocities in the nonbreaking areas are biased toward higher velocities when compared to ADV measurements. The authors relate this bias partly to the backscatter from breaking waves hit by the range and azimuth side lobes (see Section II), the latter being relatively high for the used radar setup.

Lin *et al.* [42] and Catalán *et al.* [43] studied surf zone Doppler data acquired by a coherent pulsed radar, which is very similar to the radar used in the present work. While the study of Lin *et al.* [42] focuses solely on integrated Doppler velocity and backscatter intensity data, Catalan *et al.* [43] analyzed also the range evolution of the Doppler spectra (integrated over two minutes) and the range-time evolution of the Doppler velocity modulated by shoaling and breaking waves. The results of Catalán *et al.* [43] also confirm the simultaneous occurrence of high backscatter intensities and Doppler velocities close to the phase speed associated with actively breaking waves. Thus, within the 2 minute averaging period, a single breaker is enough to completely dominate the Doppler signal.

In the present article, radar backscatter from shoaling and breaking surf zone waves is studied using a coherent-on-receive X-band pulse marine radar. In contrast to many other studies, the range-time evolution of complete Doppler spectra with high temporal resolution (0.256 s) is investigated, in addition to the integrated parameters, the backscatter intensity, and Doppler velocity. Special emphasis is put on a known, but previously unreported, consequence of the imaging principles of marine radar on the Doppler signal and its implications for its interpretation. More specifically, the range smearing effect related to the shape of the transmitted radar pulse combined with strong backscatter from actively breaking waves produces artifacts that must be considered when the signal is used to study surf zone waves.

This article is structured as follows: In Section II, a brief review of radar hardware principles and microwave backscatter theory is given. In Section III, the radar system and digital signal processing methods used in this study are described, followed by a description of the study area and obtained field data (Section IV). In Section V, the results of the analysis in terms of the bivariate probability distributions on backscatter intensity and Doppler velocity are presented and discussed. Furthermore, the consequences of radar pulse smearing on the radar measurements are highlighted in Section VI. In Section VII, the Doppler spectral evolution of a breaking wave tracked in space and time along the steepening and active breaking phase is discussed. Finally, the main conclusions and an outlook for future applications are presented.

II. Basics of Marine Radar Hydrography

The radar backscatter mechanisms relevant for oceanographic applications have been reviewed by many authors. However, the radar hardware fundamentals are often only briefly addressed. Here, we also like to mention the radar hardware fundamentals in more detail because of its relevance for the interpretation of surf zone backscatter, which is presented in Sections V and VI. The focus is hereby on marine radars, which are widely used for nautical navigation. These radars operate at X-band at grazing incidence (almost parallel to the ocean surface).

A. Hardware Fundamentals

Marine radars typically consist of a signal generation unit and an antenna. Most marine radar antennas are slotted wave guides either horizontally (HH) or vertically (VV) polarized in transmit and receive. Usually, HH polarization is used for navigation because the return signal from the ocean surface, the so-called sea clutter, is lower compared to VV. While this is desired for navigation, we believe that VV polarization is a better choice when studying the backscatter from waves. The antenna design has a direct implication on the antenna pattern, i.e., the spatial distribution of the emitted and received electromagnetic energy density. The length of the antenna influences the horizontal beam opening angle θ_{beam} and hence the azimuth resolution of the radar (typically around 1°). Longer antennas provide a better focusing of the radar beam in azimuth.

A pulsed marine radar releases electromagnetic radiation as individual pulses of a certain pulse duration τ (also called pulsewidth) at a given pulse repetition frequency (PRF). Typical pulse widths of marine radars range from 50 ns (short pulse) to 1200 ns (extra long pulse). The pulsewidth determines the range resolution and maximum coverage of a radar. Longer pulses contain more energy hence increase the maximum distance where the received backscatter stands out from the sensor's thermal noise. For hydrographic purposes, in particular for surface wave studies, a reasonably high range resolution is preferential to range coverage, hence shorter pulses are preferred. The peak pulse energy is typically between 4 kW and 40 kW. The pulsewidth (or duration) τ determines the range resolution $S_r = (c_0 \cdot \tau)/2$, where c_0 is the speed of light. S_r is the minimal distance two targets must be spaced apart from each other to be identified as individual signals. The range spacing Δr of the received backscatter depends on the sampling frequency of the analog-to-digital converter (ADC) and is usually chosen to match S_r. For example, an ADC sampling frequency of 20 MHz results in 7.5 m long-range cells in direction of the radar beam, which corresponds to a 50 ns long pulse.

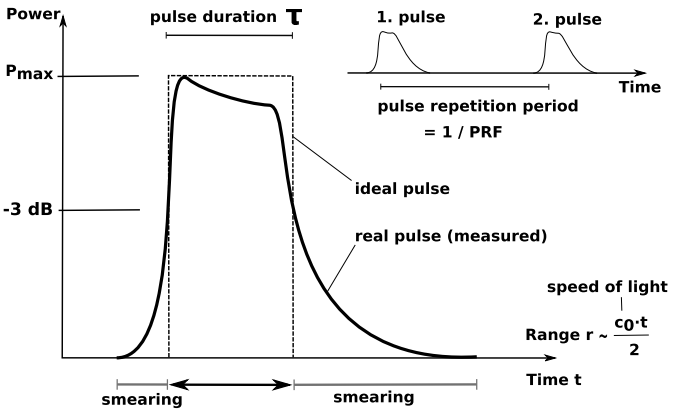

Fig. 1. Shape of the transmitted radar pulse, i.e., time evolution of the released power, with terms and definitions. The shown pulse shape is qualitatively similar as for the radar used in the present study. This was confirmed through oscilloscope measurements in the laboratory.

An ideal pulse would have an instantaneous rise and fall of the field amplitude from zero to the maximum power level and back. However, in reality it takes some time for the rise (or fall) until the power has reached the peak (or zero) power level. The pulsewidth is hence a matter of definition and is commonly defined as the time where the power level is above -3 dB of the peak power, as shown in Fig. 1). If, as explained above, Δr is chosen to match S_r for the -3 dB pulsewidth, the pulse energy below this level leaks into the adjacent range cells. In a radar image, this causes smearing in range and thus reduced sharpness. We will refer to this effect as "radar pulse smearing" throughout the rest of this article.

B. Sea Clutter

Under moderate grazing angles ($\theta_g = 10-80°$), the radar backscatter from the ocean surface is reasonably well described by the composite surface model (CSM) proposed in [44] and [45]. In the CSM, the ocean surface is decomposed into finite, slightly rough [46] surface facets with a constant inclination toward the radar. The backscatter from each facet at the ocean surface is due to Bragg resonance on waves that are of the same scale as the electromagnetic frequency of the radar radiation (e.g., [47]), i.e., centimeter scale for X-band. The Bragg model implies two modulation mechanisms (e.g., [37], [47]–[49]): tilt (local slope) and hydrodynamic modulations (longer wave orbital motions and/or currents). At low grazing angles (LGA, $\theta_g < 5°$) and high sea state, Bragg scattering poorly explains observed radar backscatter as other scattering mechanisms become important (see for example the special issue edited by Brown [50]). Non-Bragg phenomena include sea spikes, wave shadowing, and speckle.

At LGA, some areas of the ocean surface cannot be directly reached by the transmitted radiation. We refer to this effect as shadowing. In contrast to geometrical shadowing, radiation may partly diffract into wave troughs, thus "illuminating" also parts of the wave profile, that would be obscured by wave crests in camera images. Given the fact that the ocean surface geometry itself is highly nonlinear, modeling shadowing in radar images is not trivial. However, both extreme cases, a purely geometrical shadowing model [24] as well as assuming negligible influence of shadowing [51] have been proposed to be applicable to LGA backscatter, depending on the radar hardware.

Sea spikes are occasional events of very high radar backscatter intensities that are commonly attributed to steep or breaking waves (among others, [52]–[59]). Approaches to explain backscatter from breaking waves include multipath effects [60], volumetric scattering [61], or increased roughness due to bound (phase-locked) waves, which appear at the front face of a breaker [62].

C. Geophysical Interpretation of the Doppler Velocity

Any movement relative to the radar antenna of the scatterers, i.e., the roughness elements at which the signal is backscattered, causes a Doppler shift within the electromagnetic signal. The line-of sight component of the scatterer velocity, the Doppler velocity U_d, is related to the Doppler frequency shift f_d through

$$U_d = \frac{f_d \, \lambda_{\mathrm{el}}}{2 \, \cos \alpha} \tag{1}$$

where λ_{el} is the electromagnetic wavelength and α is the angle between the scatterer motion and the antenna line-of-sight.

The Doppler velocity obtained from ocean radar backscatter can be interpreted as a sum of individual components (e.g., [31]), which are influenced by either geophysical or radar imaging effects. The geophysical components include wind drift, ocean currents, surface wave orbital motions, and surface wave breaking. Nongeophysical influences are, for example, the intrinsic speed of the Bragg waves, shadowing, the geometry of the ground footprint of the radar beam, or the shape of the transmitted radar pulse.

The variation on the scale of the surface waves is mainly due to orbital motions. Wind drift and ocean currents are usually varying on longer time scales. At moderate incidence angles, U_d can be directly transformed to surface elevation through the application of wave theory [28], [37]. This is different at LGA, where the influence of non-Bragg scattering mechanisms is stronger [54]. Breaking waves can lead to high Doppler velocities close to the phase velocity of the breakers [34], [39], [63] and thus increase the observed Doppler velocity. The Doppler velocity at extreme grazing angles ($\theta_g < 3°$) contains an additional Doppler shift toward higher velocities which is most likely related to the interaction of wave nonlinearity, shadowing, and wave breaking on a subradar-resolution scale (see the introduction of [64], and references therein). This Doppler bias is not yet fully understood. Numerical experiments suggest that wave nonlinearity at the crests of small "choppy" waves has the largest influence [64]. The above-mentioned influences make the interpretation of the Doppler velocity at LGA complicated.

III. Instruments and Methods

A. Coherent-on-Receive X-Band Marine Radar

The radar used in this study is a coherent-on-receive marine radar developed at the Helmholtz-Zentrum Hereon [65]. The

radar system consists of an off-the-shelf X-band (9.48 GHz) marine radar (GEM Leonardo series) that is complemented by a dedicated processing board which was developed in cooperation with the Saint Petersburg Electrotechnical University (ETU-LETI), a high precision angle encoder, and a step-motor to steer the antenna in a fixed direction. For the present study, we used a 7.5 ft (2.286 m) wide antenna with vertical polarization in transmit and receive (VV). The radar is operated at a PRF of 2 kHz. The duration of the transmitted pulse (measured at the −3 dB power level) is between 50 and 70 ns. Pulses are generated by a magnetron with a nominal peak power of 12 kW.

The received signal runs through an ultralow noise linear amplifier before being digitized by a 4 channel 13 bit ADC. Analog-to-digital conversion is realized at 20 MHz, which corresponds to a range cell spacing of 7.5 m. A total number of 435 range cells were recorded resulting in a maximum range of 3.2 km.

B. Doppler Signal Processing

The received radar signal is coherentized during post-processing by removing the recorded phase of each transmitted pulse (coherent-on-receive). The complex coherent radar signal is then given by

$$C_{\mathrm{el}}(r, t, \theta_{\mathrm{az}}) = A_{\mathrm{el}}\ e^{i\phi_{\mathrm{el}}} \tag{2}$$

where r, t, and θ_{az} correspond to range (specifically slant range, i.e., distance from the antenna), time, and the azimuth angle (antenna view direction). $A_{\mathrm{el}} = (I_{\mathrm{sig}}^2 + Q_{\mathrm{sig}}^2)^{1/2}$ and ϕ_{el} are the amplitude and phase of the electromagnetic signal, respectively. I_{sig} and Q_{sig} are the in-phase and quadrature signals. The signal amplitude is stored in uncalibrated analog-digital-units (ADU) that are linearly related to the electromagnetic field amplitude of the received radiation.

In order to calculate the Doppler frequency shift, $n_{\mathrm{ens}} = 512$ consecutive radar pulses are aggregated in a Doppler ensemble of $\Delta t = 0.256$ s (at PRF of 2000 Hz). Doppler spectra $S_d(f)$ are computed for each ensemble using the fast Fourier transform (FFT). The Doppler shift frequency can be estimated from the first moment of the Doppler spectrum as

$$f_d = \frac{\int f\ S_d(f)\ df}{\int S_d(f)\ df}. \tag{3}$$

Occasionally, multiple peaks can appear in a Doppler spectrum. In the following, we refer to such spectra as multipeaked Doppler spectra. One reason for the occurrence of multipeaked Doppler spectra is the presence of different scattering sources on scales smaller than the radar range resolution or integration period. Each peak represents the velocity of the respective subpopulation of scatterers. Conceivable sources would be, for instance, the presence of breaking waves that only partially fill a radar cell. But also the presence of other objects such as rain, floating debris, foam, birds, or marine mammals can cause multipeaked Doppler spectra. As discussed in Section VI, also radar pulse smearing effects in combination with steep or breaking waves can cause a considerable amount of

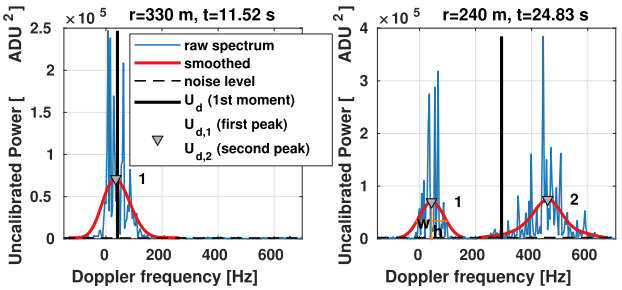

Fig. 2. Examples of a single-peaked (left) and a double-peaked (right) Doppler spectrum. Shown are raw (blue line) and smoothed (red) spectra, noise level (horizontal black dashed line), Doppler shift frequency from the first moment (vertical black line), and location of the first and second peak identified by the peak finding algorithm (gray triangles). h and w are the peak height and width at half-height. The frequency limits were chosen for better visibility. The full unambiguous range is from −1000 to 1000 Hz.

double-peaked Doppler spectra. Examples of a single-peaked and double-peaked Doppler spectrum are shown in Fig. 2.

In order to identify and separate individual peaks in the Doppler spectra, the following processing chain was applied:

1) The noise level is computed as $P_{\mathrm{noise}} = 2 \times \mathrm{median}(S_d(f))$.
2) Spectral energy below this level is removed from the spectrum prior to the peak identification.
3) The spectra are smoothed using a moving average scheme that is repeated 3 times. The window span for the moving average was 17 discrete frequency bins corresponding to 66.4 Hz.
4) Doppler peaks are identified from the smoothed spectra using the function FINDPEAKS from MATLAB's signal processing toolbox. No more than three peaks are allowed to be identified by the peak finder. The width w of a peak is defined as the span of the peak at half of its height h (see Fig. 2). If $h < 3\ P_{\mathrm{noise}}$, the peak is discarded. For each identified peak, its frequency, width w, and height h are determined.

Intensity and Doppler Velocity: We compute the backscatter intensity and Doppler velocity using two different definitions:

1) The backscatter intensity I is the total received power, i.e., the zeroth moment of the Doppler spectrum. The corresponding Doppler velocity U_d (vertical black lines in Fig. 2) is derived from the first moment using 3 and 1.
2) For each identified peak, the intensity is estimated as $I_i = w_i\ h_i$, where $i = 1, 2, 3$. The location of the peak defines its Doppler shift frequency and respective Doppler velocity $U_{d,i}$.

The first-moment Doppler velocity U_d is the most common definition which is often called the Doppler centroid. For single-peaked Doppler spectra, $U_{d,1}$ and U_d are almost identical (left plot in Fig. 2). However, $U_{d,i}$ may be a better choice for the correct interpretation of the geophysical contributions to the Doppler spectra, as discussed in more detail later.

C. Terminology

Throughout the rest of this article, the term "peak" refers to peaks inside individual Doppler spectra, and peaks inside

the joint distributions of backscatter intensity and Doppler velocity (analyzed in Section V) are called "modes." Doppler peaks (if present in the spectra) are called "first," "second," or "third" Doppler peaks (starting from left to right, or from low to high velocity). "Multipeaked" Doppler spectra are spectra where more than one peak was detected. The terms "slow" and "fast" refer to the absolute Doppler velocity below or above the adaptive velocity threshold that is described in Section VI.

IV. Field Observations

A. Study Area and Field Instrumentation

The Helmholtz–Zentrum Hereon operates a shore-based, long-term radar station at the west coast of the island of Sylt, Germany (54.7903°N, 8.2833°E) as part of the Coastal Observing System for Northern and Arctic Seas (COSYNA, see [66]). A directional wave rider buoy (Datawell DWR-MkIII) is located ≈1 km off the coast (54.790°N, 8.267°E) in a water depth of 10 m.

Sylt is a narrow barrier island in the German Bight separating the North Sea from the intertidal mudflats of the North Frisian Wadden Sea. The western coastline is a mesotidal, sandy, mixed energy coast, equally influenced by tidal currents, and wave action. The shoreline at the study area is oriented northward with a small inclination of 2° with respect to north. Wind waves are predominantly approaching the island shore-normal from west, which was also the case during the study period. Low-energetic swells typically come from the northwest.

The bathymetry was measured during September 22–26, 2016, using a 210 kHz single beam echo sounder. The data were tide corrected using precise differential GPS positioning. This dataset and further details about data acquisition and quality control are available from the PANGEA data portal [67]. For the present study, these data were mapped onto a 5 m × 5 m grid by averaging all data points within one grid cell along the shore-normal profile in front of the radar station. The beach profile shows an intertidal sandbar roughly at a distance of 150 m from the radar and a second, subtidal sandbar at a distance of 500 m [see Fig. 3(d)].

B. Radar Data: Space-Time Diagrams

For the present study, we restrict our analysis to one single radar record of 10 min, starting at the September 29, 2016, 22:11:19 UTC, with the radar antenna pointing in a fixed direction along the cross-shore transect toward the wave rider buoy ($\theta_{\mathrm{az}} = 271°$). The wind speed measured at the station was 19 m/s from West. The wave rider buoy measured a significant wave height of $H_s = 3.2$ m and a peak wave period of $T_p = 10$ s. The peak direction of the wave field was $\theta_p = 280°$ (nautical convention), and the tidal elevation $\zeta = 1.61$ m (indicated by the blue solid line in Fig. 3). Wind and waves were thus approaching the coast almost shore-normal and the radar antenna was pointing into the wind.

Fig. 3 shows the time-range diagrams of backscatter intensity and Doppler velocity for the given radar record. The backscatter intensity is given in an uncalibrated relative logarithmic scale (1 dB = 20 $\log_{10}(A_{\mathrm{el}}/(1\ \mathrm{ADU}))$). Projection

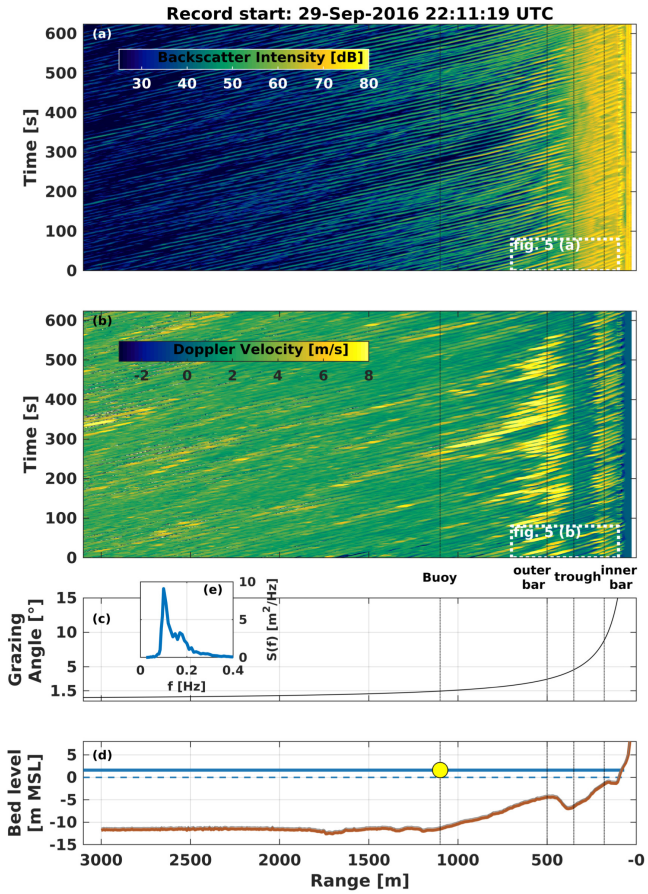

Fig. 3. Time-range diagram of (a) measured backscatter intensity I and (b) first moment Doppler velocity U_d for the 10-min long radar record with fix-pointing antenna, (c) still water grazing angle θ_g, (d) beach profile. Dashed vertical lines indicate the locations of the stations "inner bar" ($r = 180$ m), "trough" ($r = 350$ m), "outer bar" ($r = 500$ m), and "buoy" ($r = 1100$ m). Panel (e) shows the surface wave spectrum observed by the wave rider buoy.

effects are neglected because the angle between the peak wave direction ($\theta_p = 280°$) and the antenna line-of-sight ($\theta_{\mathrm{az}} = 271°$) was <10°, which is in the same range as the directional accuracy of the buoy and corresponds to a projection error of about 1.5% ($\cos(10°) = 0.985$). The stripe-like pattern in Fig. 3(a) and (b) is due to the modulation of I and U_d by waves traveling toward the shoreline. The shoreline is located approximately at $r = 55$ m. Two breaker zones are clearly visible. They appear as bright (high power) and fast (high Doppler) pixels within the range-time images. The first one (seen from offshore) spans from $r = 750$ m to $r = 380$ and the second one from m $r = 230$ m to $r = 70$ m. This corresponds to the location of the sandbars [see the bathymetry transect in Fig. 3(d)].

V. Bivariate Probability Distribution

For further investigation, the bivariate probability distributions of backscatter intensity and Doppler velocity were computed at different stations along the radar view direction (i.e., the cross-shore transect). We selected four characteristic locations at the "inner bar" at $r = 180$ m, the "trough" at $r = 350$ m, the "outer bar" at $r = 500$ m and the "buoy"

at $r = 1100$ m, representing different wave conditions and grazing angles. These locations are indicated by the vertical black lines in Fig. 3. The results are shown in Fig. 4 in terms of empirical joint probability density functions (JPDF). For each plot in Fig. 4, three adjacent range cells (± 1) were compiled to one sample with a sample size of $N = 7314$. The bin sizes used to compute the JPDFs were 0.2 m/s and 1 dB, for velocity and intensity, respectively. The columns Fig. 4 correspond to the different locations and the rows to the different definitions of the backscatter intensity and Doppler velocity (I and U_d, I_1 and $U_{d,1}$, I_2 and $U_{d,2}$, as defined in Section III-B).

For the top row [Fig. 4(a)–(d)], the intensity I and Doppler velocity U_d were computed from the zeroth and first spectral moment of the Doppler spectra (see Section III-B) and thus it is similar to Fig. 3 of Farguharson *et al.* [41], who also studied power weighted Doppler velocities, but for a FMCW radar system. For all other panels, the intensity and Doppler velocity are computed by identifying individual peaks inside the Doppler spectra (using the peak separation algorithm introduced in III-B, shown as triangles in Fig. 2). For simplicity, we restrict our analysis to the first two peaks (from slow to fast) inside a Doppler spectrum. The middle row corresponds to the first peak quantities (I_1 and $U_{d,1}$), whereas the bottom row to the second peak (I_2 and $U_{d,2}$). Note that the first peak is always present if the signal is above the noise floor, while the second peak appears occasionally. In both cases, the probability density is computed relative to the total number of Doppler ensembles (regardless of how many peaks are present in each ensemble).

Inside the breaker zones, at the intertidal sandbar (inner bar) and the subtidal sandbar (outer bar), the JPDFs [Fig. 4(a) and (c)] indicate a clear bimodal distribution of I and U_d. One mode is observed with relatively slow Doppler velocities and low backscatter intensities. A second mode has intensity values, that are more than 10 dB higher compared to the first mode, as well as high Doppler velocities close to the phase velocity of shallow water waves (i.e., $c_{p,\mathrm{sw}} = (gd)^{1/2}$, where d is the water depth and g is the gravitational acceleration). The dashed vertical lines refer to $(gd)^{1/2}$. The solid lines and the dashed horizontal line are explained in Section VI. This confirms the expected appearance of distinct modes reflecting different types of scatterers in the surf zone. The fast mode is due to scatterers that are phase-bound to the breaking waves carrying them and the slow mode is due to nonbreaking scatterers, i.e., the Bragg waves (e.g., [41]).

At the inner bar, there seems to be a sharp cutoff at the highest intensity values [Fig. 4(a)]. This cutoff is even more pronounced for the distribution of the first peak intensity I_1 which is shown in Fig. 4(e). This is most likely due to the fact that the signal runs into saturation for the strongest scatterers present. The largest percentage of sensor saturation was found at the inner bar, where $\approx$16% of the raw pulses are saturated in one channel. At the outer bar, the percentage of saturated pulses is $<$2%. Further offshore or in the absence of breaking, saturation hardly occurs ($<$0.1%). The influence of saturation on the estimation of the Doppler velocity was estimated through idealized simulations of partially saturated Doppler ensembles. It was found (not shown) that saturation lowers the signal-to-noise ratio and, even if this may induce uncertainty, the effect on the integrated Doppler velocity was negligible. Therefore, the findings of the present study are not affected by saturation.

With increasing range and decreasing grazing angle, more and more Doppler ensembles appear on the low intensity tail of the distribution for both, the breaking and the nonbreaking mode. One conceivable reason for this is that radar some range cells are partially shadowed. This would lower the observed intensity proportional to the percentage of the range cell occupied by shadowing. The dependence on the grazing angle supports this hypothesis, but more data is needed to validate it.

The first peak intensity I_1 and Doppler velocity $U_{d,1}$ [Fig. 4(e) and (f)] are in general very similar to the JPDFs in the top row [Fig. 4(a)–(f)]. However, at the inner bar, the two modes (breaking and nonbreaking) are apparently more clearly separated [Fig. 4(a) compared to (e)]. This is different at the outer bar, where there is no clear difference between the JPDFs with or without peak separation [Fig. 4 (c) versus (g)]. The observed differences are most likely due to radar pulse smearing in combination with strongly backscattering breaking waves and shadowing, which will be shown and discussed in Section VI.

Regardless of the definition of the intensity and Doppler velocity, all four stations show some ensembles in a third mode with Doppler velocities around 4.5 (± 2) m/s [Fig. 4(a)–(h)]. The corresponding range of intensities spans over the complete intensity range of the nonbreaking mode. A few ensembles show intensity values that are much higher than the nonbreaking mode, but still lower than the breaking mode. Possible reasons for this could be either the appearance of smaller breakers (whitecaps), which do not fill a complete radar cell but still increase the intensity and Doppler velocity, or huge and strongly backscattering breaking waves that are hit by side lobes. However, a clear attribution of the origin of such Doppler ensembles is beyond the scope of the present study.

Panels (i)–(l) of Fig. 4 show the JPDFs for the second Doppler peaks (I_2 and $U_{d,2}$), in case where they are present in the Doppler spectrum. At the inner and outer bar [(i) and (k)], fast peaks mostly show velocities similar to the breaking mode which was observed in (a), (e), (c), and (g), but with a significantly lower intensity. However, at the trough (j) and the bouy (l), second Doppler peaks have velocities around 4.5 (± 2) m/s, which is the range of speeds of the third mode mentioned in the paragraph before. In fact, this third mode and corresponding second Doppler peaks are also apparent at the two breaker bars [panels (i) and (k)]. The appearance of second Doppler peaks is related to the presence of multiple sources of scattering within one range cell, e.g., Bragg waves and bound waves at the crest of breaking waves [62]. However, radar pulse smearing can also cause multipeaked Doppler spectra. This effect is analyzed in detail in the following Section VI.

VI. Breaking Waves and Radar Pulse Smearing

As described above, two major modes appear in the JPDFs of intensity and Doppler velocity at both breaker zones.

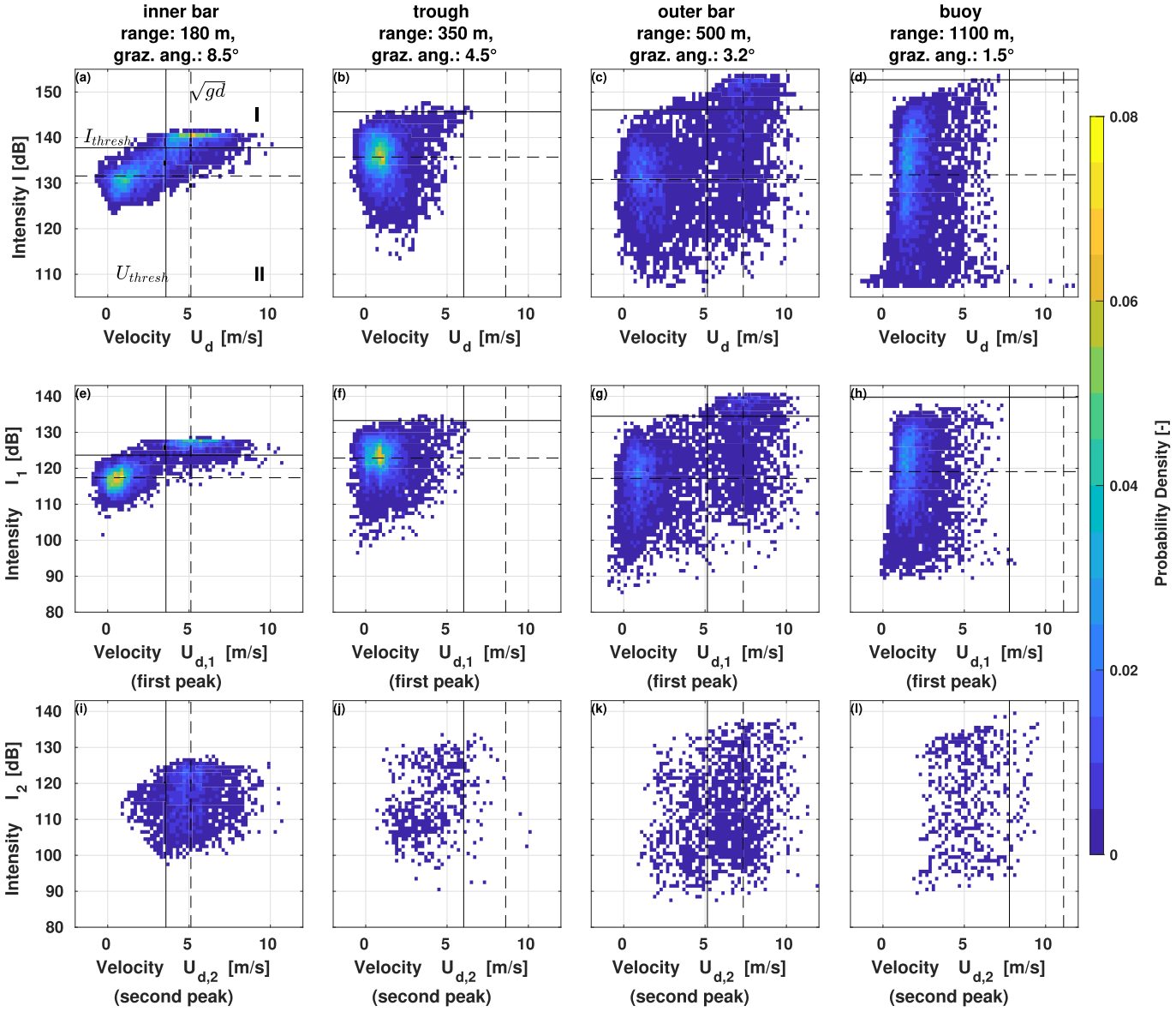

Fig. 4. Joint Probability Distributions of backscatter intensity ($I\,r^3$, corrected for range spreading loss which is $\propto r^{-3}$) and Doppler velocity computed from the zeroth and first moments Doppler spectra [I and U_d, (a)–(d)], from the first Doppler peaks [I_1 and $U_{d,1}$, (e)–(h)] and from the second Doppler peaks [I_2 and $U_{d,2}$, (i)–(l)]. Bin sizes are 1 dB for the intensity and 0.2 m/s for the Doppler velocity. The sample size of each JPDF is $N = 7314$. The columns refer to the locations marked in Fig. 3.

A relatively slow (nonbreaking) mode and a fast (breaking) mode. Especially at the outer bar, a considerable amount of fast Doppler ensembles show intensity values, that are of the same magnitude as the slow (nonbreaking) mode, but with similar Doppler velocities as the breaking mode. Such fast and weak scatterers cannot be explained by scattering theory alone (without considering further aspects of radar imaging). In the following, we will therefore analyze and discuss this feature and show evidence that this can be addressed to radar pulse smearing at LGAs.

A. Occurrence of Fast or Multipeaked Doppler Spectra

To investigate the occurrence of fast Doppler ensembles, we first split the sample into two subsamples based on the Doppler velocity relative to the shallow water phase velocity: slow Doppler ensembles, with $U_d \leq 0.7(gd)^{1/2}$, and fast Doppler ensembles, with $U_d > 0.7(gd)^{1/2}$. The velocity threshold $U_{\text{thresh}} = 0.7(gd)^{1/2}$ is selected here because it roughly matches the location of the local minimum in the Doppler velocity histograms throughout the whole surf zone. Moreover, with the assumption that the observed Doppler velocity roughly resembles the horizontal surface velocity, this threshold is similar to the well-known kinematic breaking criterion (e.g., [68], where 0.85 was used). The fast subsample was then again separated into two classes: Class I consists of fast Doppler ensembles with a high backscatter intensity, class II of fast Doppler ensembles with low intensity. The intensity threshold I_{thresh} is defined as the median plus two standard deviations of the slow ensembles (where $U_d < 0.7(gd)^{1/2}$).

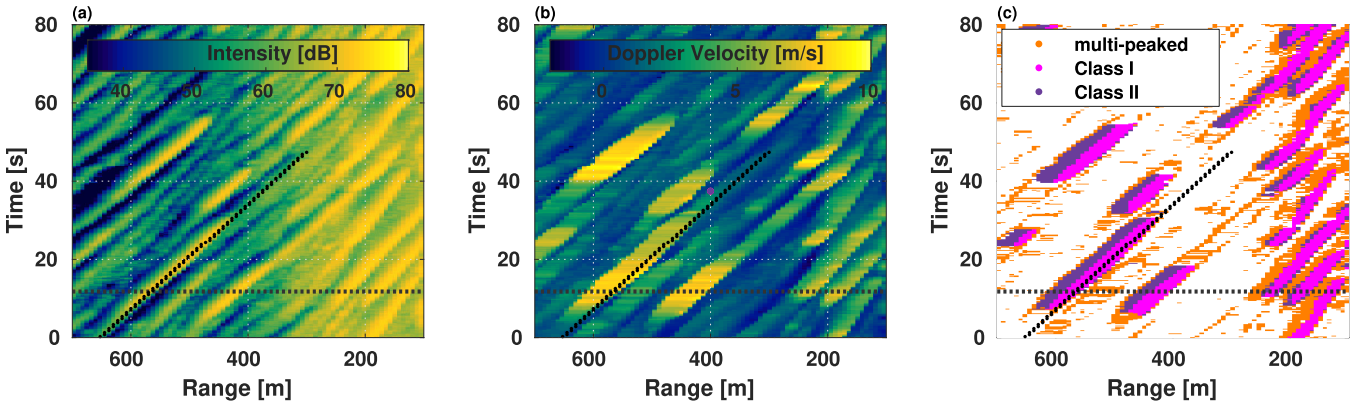

Fig. 5. Zoom of the space-time diagram (white rectangle in Fig. 3) of (a) backscatter intensity, (b) Doppler velocity and (c) location of ensembles with high intensity (Class I), fast ensembles with low intensity (Class II) and multipeaked spectra. The dotted horizontal lines show the location of the Doppler spectra shown in Fig. 6, inclined dotted lines to the tracked breaker shown in Fig. 8.

The classes are labeled in the JPDFs shown in Fig. 4, where the solid black lines indicate the adaptive intensity and velocity thresholds used for the conditional analysis of the sample at each station. The horizontal dashed lines in Fig. 4(a)–(h) show the median intensity value of the slow ensembles. For the inner bar and trough, the median matches the most frequent values of the slow mode in the JPDFs. However, at the outer bar and the buoy it does not match anymore with the most frequent value of the slow mode and the distribution becomes wider in terms of intensity with increasing range. In terms of Doppler velocity, however, the breaking mode is relatively symmetric around its most frequently observed velocity (at $(gd)^{1/2}$, or slightly faster).

In order to investigate where and when fast Doppler ensembles or multipeaked Doppler spectra appear, a zoom of the range-time diagram of backscatter intensity and Doppler velocity is shown in Fig. 5. The third range-time plot shows the location of Doppler ensembles with high intensity (Class I), fast ensembles with low intensity (Class II), and multipeaked spectra. Two major peculiarities can be noticed in this figure:

1) The fast but weak (class II) ensembles appear almost exclusively behind the fast and strong (class I) ensembles, which stem from dominant breakers.
2) The spatial extent of the class II area is much larger at the outer bar (350 m $< r <$ 650 m).

In the absence of fast objects in the air e.g., birds, strong rain, hail, or snow, the Doppler ensembles in class I are caused by the dominant actively breaking waves of the wave field. This is consistent with the findings of [41]. However, this does not explain the class II ensembles, which are fast but have moderate to low backscatter intensities. The fact that class II accumulates behind class I and is more frequently observed at the outer bar is a strong indication that the reason for the class II is radar pulse smearing in combination with shadowing behind the steep breaking waves, as shown below.

B. Spatial Extent of Breaking Wave Doppler Signatures

To gain further insight into the spatial characteristics of the Doppler signal, we studied the range distribution of the Doppler spectra at a given time $t = 11.776$ s, when multiple breaking waves at different distances were present. Fig. 6 shows the normalized Doppler spectra corresponding to each pixel along the dotted horizontal line in Fig. 5.

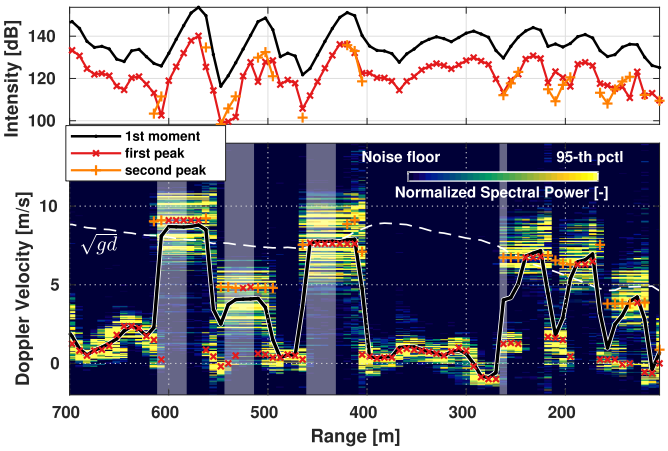

Fig. 6. Range distribution of Doppler spectra at $t = 11.776$ s (along the dotted horizontal line in Fig. 5). Each spectrum is normalized between 0 and the individual maximum spectral power. The backscatter intensity is shown in the upper panel. Colors in the upper (lower) panel correspond to I (U), I_1 ($U_{d,1}$), and I_2 ($U_{d,2}$), which are first moment, and the first and second Doppler peak, respectively. The whitened areas indicate "similar and decaying" Doppler spectra as defined in Section VI-C.

Six potential breakers show up as regions with increased velocity and intensity, three at the inner bar and three at the outer bar. While for most breakers, the Doppler velocity is close to the shallow water phase velocity $(gd)^{1/2}$, the event at roughly $r = 525$ m shows a slower Doppler velocity around 4.5 m/s. As it can be seen in Fig. 5, this event does not contain any class I ensembles, because the Doppler velocity does not exceed the velocity threshold of $0.7(gd)^{1/2}$. This event could be either a breaking shorter wave riding on the dominant longer waves and breaking is due to steepening caused by the longer waves, or the wave is only steepening over the outer sandbar then deshaols and breaks later at the inner bar at roughly $r \approx 250$ m.

The dominant scatterers of active breakers are mainly droplets surfing down the front face of the waves. Their velocity distribution, and hence the Doppler spectral width, is much broader than the one of the nonbreaking surface, where most scatters move at similar speeds.

Furthermore, the spatial extent of the breaking waves signatures is between 6 and 9 cells corresponding to 45 to 67.5 m in range. The dominant waves ($T = 10$ s) have a wavelength of 92 m at 10 m water depth, or 10 m at 3 m, respectively. Thus, the fast moving region spans over more than 60 to 90% of the wavelength. This seems unrealistically large as in other observational studies [69]–[72] the reported extent of surface rollers (i.e., the turbulent, fast moving air-water mixture at the front face or breaking waves) is only a small fraction of the wavelength.

The three individual breakers at the outer bar seem to differ only in the leading part of the signature. Farther behind, the (normalized) spectra are almost identical to the preceding radar cells. At the same time, the intensity drops by about 5 dB from one range cell to the next. The high spectral similarity and rapidly decaying backscatter intensity are a strong indication that this can be attributed to radar pulse smearing (see Section II). Let us consider a realistic pulse shape such as the one sketched in Fig. 1, with a pulselength (at the -3 dB level) of $\tau = 50$ ns. The shape of this pulse is qualitatively similar to the measured pulses for the radar that is used for the present study. There is also energy left below the -3 dB level. This pulse energy leaks into the adjacent cells and thus the total time a (small) target at a given location would be affected by the energy of a single pulse is significantly longer than for an ideal pulse shape (approx. 130 ns for the sketched pulse). Thus, the target will be mapped to more than one range cell in the recorded backscatter image. If the next range cell has a very low return signal, for example, due to shadowing, the leaked energy due to radar pulse smearing of the preceding range cell is high enough to dominate the Doppler spectrum. This causes very similar spectra with a strong range decay of the backscatter intensity.

At the inner bar ($r < 250$ m), this behavior is different. Here, the grazing angle is higher (8.5° versus 3.2°) and hence the expected amount of shadowing lower. Surf zone waves are asymmetric about the vertical axis (e.g., [73]). Thus, the larger part of the wave profile has a negative slope. Moreover, turbulence generated by the breakers can destroy surface roughness behind breakers. As demonstrated recently for a Ka-band scatterometer in a wave flume [74], this effect can lead to a very low backscatter intensity in this region, even if it is not geometrically shadowed. Therefore, the smeared signal from the preceding range cell is usually strong enough to produce a noticeable signal and appears as a second Doppler peak in the succeeding range cells. For 3 to 4 range cells, both the slow and the fast peaks inside the Doppler spectra are of similar magnitudes [which can be seen from the red and orange lines in Fig. 6(a)]. The fast and broad Doppler signal, most likely resulting from active breaking, shows a similar range behavior as the one observed at the outer bar, where the signal from the nonbreaking surface is not strong enough to cause a Doppler peak. The slow Doppler peaks are in the range of the orbital motion of waves and thus mostly represent the velocity of the nonbreaking surface. However, at large grazing angles, breaking signatures are not restricted to fast peaks [75]. Instead, some parts of the breakers show Doppler velocities close to the orbital velocity, while at lower grazing angles the breaking Doppler velocity is close to the phase velocity breakers. The difference between the signatures at the inner bar and the outer bar further confirms this finding.

The black line in Fig. 6(b) corresponds to the first-moment Doppler velocity U_d (i.e., the power weighted average of scatterer velocity). In some parts of the wave profile, U_d will neither represent the speed of the breaking parts, nor the nonbreaking, but yield something in between. However, if the true signal from the surface is still strong enough to cause a distinct peak in the Doppler spectrum, the peak separation can help to recover both, the smeared and the true signal.

Second peaks ($U_{d,2}$, orange crosses) appear primarily at the edges of the breakers. The second peaks have similar Doppler velocities as the fast first peaks ($U_{d,1} > 0.7(gd)^{1/2}$). This suggests that the nonbreaking surface is still strong enough to induce a distinct peak, until the point when the fast breaking scatterers dominate the spectrum. Then the first peak (which then is a fast peak) is the only detectable peak inside the Doppler spectrum, and breaking scatterers dominate the spectrum. The first peak Doppler velocity ($U_{d,1}$) jumps from the level of the slow scatterers to the velocity of the fast scatterers within one range cell. Note that the first moment Doppler velocity U_d [black line in Fig. 6(b)], also changes from slow to fast, but the the transition happens much more gradually. This is due to the fact that U_d represents a mix between both populations of scatterers. The extent of this smoothing effect will depend on the range resolution of the radar. This shows nicely that the peak separation algorithm introduced in Section III-B makes it possible to detect the sharp increase of the Doppler velocity at the leading edge of a breaking wave, even if the recorded signal is oversampled in range. On the contrary, the interpretation of the transition from fast to slow scatterers at the trailing edges is more difficult due to the influence of shadowing and the signal attenuation due to turbulence, which was mentioned before.

C. Percentage of Unrecognized Shadowing

For quantitative analysis, the occurrences of radar pulse smearing and shadowing were detected by comparing one Doppler spectrum to its predecessor in range. Different spectral similarity measures were tested. The correlation of the spectral power of the frequency bins of the Doppler spectra after smoothing the spectra with a moving average filter spanning over 5 frequency bins yielded the best results. The applied filter is equivalent to reducing the number of samples used to compute the spectra, thus reducing the frequency resolution. "Similar and decaying" spectra are defined as spectra with a very high correlation ($r > 0.98$) and a decrease in backscatter intensity by more than 4 dB compared to the preceding range cell. The whitened regions in Fig. 6 mark all of those Doppler spectra. Fig. 7 shows the space-time diagram for the first 250 s of the measurement, where "similar and decaying" spectra

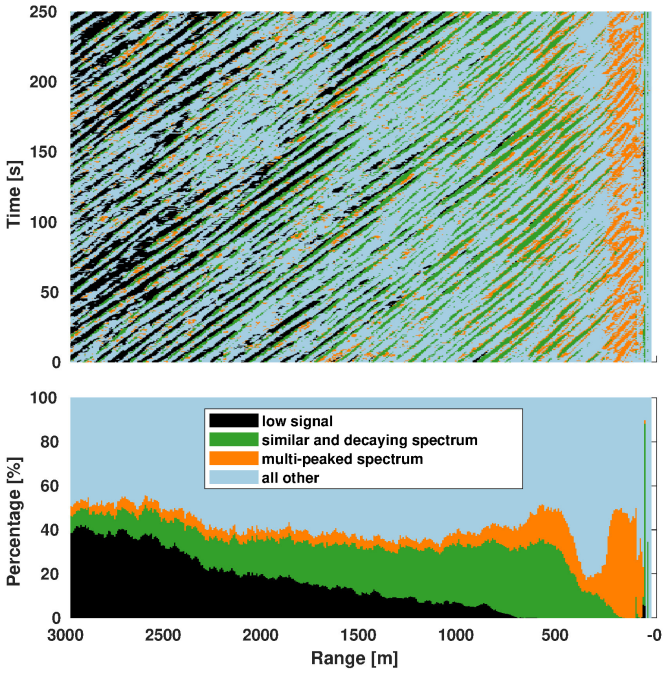

Fig. 7. Space-time diagram (first 250 s) with colorized pixels where the spectra are similar and decaying (green), the return signal is low (SNR < 3 dB, black) or the Doppler spectrum is multipeaked (orange). The lower panel shows a stacked bar visualization of the relative occurrence at each range cell over the entire 600 s of measurement.

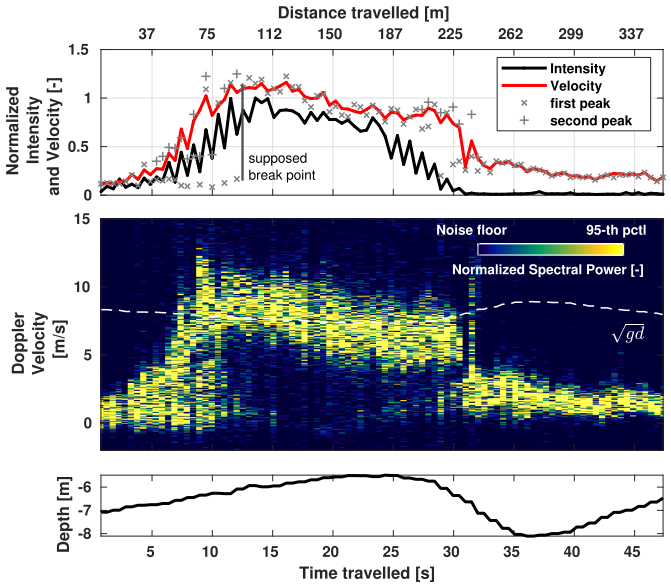

Fig. 8. Space-time evolution of Doppler parameters for a manually tracked individual breaking wave. The top panel shows the backscatter intensity (black) and Doppler velocity (red), normalized by the maximum intensity (2.4726 10^{15} ADU^2) and phase speed (7.48 m/s) of the breaker during the trace. Also shown are normalized Doppler spectra (middle panel) and the water depth (bottom panel).

are indicated by green color. Black pixels indicate where the signal is low compared to the average amplitude of sensor noise $A_{\mathrm{el,noise}} = 8$ ADU and SNR $= 20\log_{10}(A_{\mathrm{el}}/A_{\mathrm{el,noise}}) <$ 3 dB. Orange pixels indicate multipeaked Doppler spectra. The lower plot shows a stacked bar visualization of the relative occurrences of such "similar and decaying", "low signal," and "multipeaked" spectra for each range cell, considering the entire sample of 600 s.

In the very far range ($r > 2500$ m), about 40% of the Doppler ensembles have a low return signal and another 10% are similar and decaying spectra. At range $r = 1500$ m, "low signal" and "similar and decaying" ensembles (black and green pixels) together account for roughly 40% of the samples.

At the crest of the outer bar ($r \approx 500$ m), no "low signal" pixels are detected. However, the percentage of "similar and decaying" spectra is still up to 50% at this location. Roughly 10% of the Doppler spectra at this location are "multipeaked" (orange pixels), where the power weighted (first moment) Doppler velocity neither represents the nonbreaking nor the breaking surface Doppler velocity, but the correct Doppler velocity can be recovered through peak separation (see Section VI-B). However, the "similar and decaying" spectra are artifacts due to radar pulse smearing and the Doppler velocity must be discarded. At the inner bar ($r < 250$ m), the share of pulse smearing artifacts is negligible, but the multipeaked spectra still cover 50% of the measurements. Thus half of the Doppler velocities would be biased, if the traditional Doppler velocity U_d is considered, instead of $U_{d,1}$ which is obtained through peak separation.

At both breaker bars, the percentage of orange pixels is increased. This shows that wave breaking significantly increases the occurrence of multipeaked spectra. Another apparent feature here is the drop in the amount of green pixels between $r = 500$ m and $r = 400$ m. Wave breaking reduces the wave height and, if the water depth does not change, also the mean wave steepness (i.e., the ratio between wave height and wavelength). This behavior strengthens our hypothesis that "similar and decaying" ensembles are artifacts and should be considered as "unrecognized" shadowing, which depends directly on wave steepness.

In summary, Fig. 7 shows that the amount of valid data depends not only on the local grazing angle and wave steepness but also on the occurrence of wave breaking and the pulse properties of the used marine radar. For this particular radar system and environmental conditions, the percentage of multipeaked Doppler spectra is roughly 50% at the inner bar and 20% at the outer bar. This means that the power weighted Doppler velocity without peak separation would yield unbiased Doppler velocities for only 50% of the measurements at both breaker bars.

VII. Recommendations for Studying Individual Breakers

The biggest advantage of marine radar remote sensing is its ability to trace features in space and time. Of special interest for the study of nearshore waves is the space-time evolution of individual shoaling waves passing different stages of wave breaking, i.e., steepening, active breaking, and post-breaking. To avoid unwanted influences of the radar imaging, we want to make two main recommendations for fixed antennas looking into the main wave direction of a shoaling wave field:

1) Doppler peak separation should be used to obtain the Doppler velocity.
2) The study should be restricted to the front faces (leading parts) of the waves, where the wave profile is completely "illuminated" by the radar radiation.

Fig. 8 shows the space-time evolution of the Doppler spectra of a breaking wave tracked along its path. The track is assumed to be linear, i.e., at constant speed. It was chosen by visual inspection of the range-time diagram (black dots in Fig. 5). The evolution of the backscatter intensity and (first moment) Doppler velocity are remarkably similar to each other. Both show a rapid increase over 5 s until the Doppler velocity reaches its maximum at about 1.2 times the phase speed. We believe that the rapid increase represents the steepening phase of the wave, active breaking starts at the local maximum (at $\approx$12 s) and lasts for roughly 15 s. After that, it takes another 5 s until the breaking signature vanishes from the backscatter. The observed space-time Doppler signatures are generally very similar to the laboratory radar measurements by [76]. This supports our hypothesis about the different breaking stages but must be further validated in the future, for example, through collocated video analysis.

Also worth noting is the evolution of the Doppler spectra. Within the steepening phase, the Doppler spectra broaden significantly and there are no clear Doppler peaks visible in that region. However, the first moment Doppler velocity follows faster parts of the spectra. This indicates that the signal from breaking is always strong enough to dominate the backscatter, even if the nonbreaking surface appears as a distinct slower peak. During wave steepening and before breaking terminates, the Doppler spectra still contain information on the nonbreaking surface, which can be recovered through Doppler peak separation.

VIII. Summary and Conclusion

We have presented a detailed study of the coherent microwave backscatter from shoaling and breaking waves measured with a shore-based coherent-on-receive marine radar. The radar was located on a dune cliff at a height of 28 m above mean sea level, yielding near to LGAs for the vast majority of the dataset. The antenna was pointing into the main wind and wave direction, which was perpendicular to the coast line. We focused on a 10 minute radar record during a locally generated storm sea state with significant wave heights of up to 3 m and a peak wave period of 10 s. The dataset covers a maximum distance of 3 km, whereas the main focus of our study is on the first 1000 m, where the wave field propagates over a subtidal and an intertidal breaker bar toward shore.

Consistent with previously reported findings [41], the dominant depth-induced breaking waves show up as a distinct mode in the JPDFs of backscatter intensity and Doppler velocity. The backscatter intensity of breaking Doppler ensembles is about 10 dB higher compared to nonbreaking ensembles and the Doppler velocity at breaking is close to the shallow water phase velocity of the waves.

We put special emphasis on the consequences of radar imaging effects, particularly radar pulse smearing, on the resulting backscatter signal and its interpretation. Pulse smearing causes artifacts that appear in areas where the radar pulse cannot be directly transmitted to the surface because of sheltering by preceding waves. In these cases, the remaining energy of the preceding radar range cell is often still large enough to influence or even dominate the Doppler signal in the succeeding cells. Because a "low signal" threshold alone is not able to identify such Doppler ensembles, we call this "unrecognized" shadowing and propose a combined threshold by comparing the Doppler spectra of adjacent range cells: a strong range signal loss ($>$4 dB) and a high spectral similarity ($r > 0.98$). This combined threshold allows for an automated detection of radar pulse smearing artifacts. For the present dataset, unrecognized shadowing affects up to 40% of the observed Doppler ensembles and depends on the local grazing angle and most likely on wave steepness. The actual share of "unrecognized" versus "recognized" (as low signal) shadowing is also expected to depend on the used marine radar hardware, in particular the shape and peak power of the transmitted pulse.

Both, wave breaking and radar pulse smearing are a source for multipeaked Doppler spectra. For such spectra, the Doppler velocity estimated from the first moment (i.e., the power weighted average) neither represents the velocity of the nonbreaking nor the speed of the breaking surface scatterers. However, a clear distinction between valid multipeaked spectra, where breaking and non-breaking is actually present within the radar cell, and radar pulse smearing artifacts requires further investigation. Conducting a Doppler peak separation during processing of the raw data allows for the reconstruction of the nonbreaking surface scatterer velocity, as long as the signal can reach the surface behind the breaker and the nonbreaking surface produces a peak in the Doppler spectrum. Otherwise, the strong signal from breaking that leaks into adjacent range cells due to radar pulse smearing dominates the Doppler spectrum.

We, therefore, recommend to restrict the analysis of surf zone backscatter to the well-illuminated front faces of the waves and to conduct peak separation, if shore-based pulsed marine radar is used to study surf zone waves. Careful analysis of the space-time evolution of the Doppler spectra along a tracked breaking wave crest revealed high potential to identify different stages (steepening, active breaking, and termination) of wave breaking.

Acknowledgment

The authors would like to thank J. Bödewadt and J. Stell for providing essential technical support for the operation and maintenance of the radar station. Code and data to reproduce the figures of this article are available from https://doi.org/10.5281/zenodo.5068511. The following functions have helped to improve the appearance and quality of the figures: HCPARULA by Yong Hoon Lee [79], IMAGESCNAN by Carlos Adrian Vargas Aguilera [77] and EXPORT_FIG by Yair Altman [78]. The authors would like to thank the developers for making their code available.

REFERENCES

[1] I. A. Svendsen, *Introduction to Nearshore Hydrodynamics* (Advanced Series on Ocean Engineering), vol. 24. Singapore: World Scientific, Dec. 2005. [Online]. Available: https://www.worldscientific.com/worldscibooks/10.1142/5740

[2] R. A. Dalrymple, J. H. MacMahan, A. J. Reniers, and V. Nelko, "Rip currents," *Annu. Rev. Fluid Mech.*, vol. 43, no. 1, pp. 551–581, 2011, doi: 10.1146/annurev-fluid-122109-160733.

[3] H. Oumeraci, P. Klammer, and H. W. Partenscky, "Classification of breaking wave loads on vertical structures," *J. Waterway, Port, Coastal, Ocean Eng.*, vol. 119, no. 4, pp. 381–397, Jul. 1993. [Online]. Available: https://ascelibrary.org/doi/abs/10.1061/%28ASCE%290733-950X%281993%29119%3A4%28381%29

[4] T. Aagaard and S. G. Jensen, "Sediment concentration and vertical mixing under breaking waves," *Mar. Geol.*, vol. 336, pp. 146–159, Feb. 2013, doi: 10.1016/j.margeo.2012.11.015.

[5] K. W. Inch, "Surf zone hydrodynamics: Measuring waves and currents," in *Geomorphological Techniques*, vol. 3, S. Cook, L. Clarke, and J. Nield, Eds. London, U.K.: British Society for Geomorphology, Jun. 2014, ch. 3, pp. 1–13. [Online]. Available: http://geomorphology.org.uk/sites/default/files/geom_tech_chapters/3.2.3_SurfZoneHydrodynamics.pdf

[6] A. D. Short and D. W. Jackson, "Beach morphodynamics," *Treatise Geomorphol.*, vol. 10, pp. 106–129, Oct. 2013.

[7] R. Holman and M. C. Haller, "Remote sensing of the nearshore," *Annu. Rev. Mar. Sci.*, vol. 5, pp. 95–113, Jan. 2013, doi: 10.1146/annurev-marine-121211-172408.

[8] P. S. Bell, "Shallow water bathymetry derived from an analysis of X-band marine radar images of waves," *Coastal Eng.*, vol. 37, nos. 3–4, pp. 513–527, Aug. 1999. [Online]. Available: https://linkinghub.elsevier.com/retrieve/pii/S0378383999000411

[9] P. S. Bell and J. C. Osler, "Mapping bathymetry using X-band marine radar data recorded from a moving vessel," *Ocean Dyn.*, vol. 61, no. 12, pp. 2141–2156, Dec. 2011.

[10] G. Ludeno *et al.*, "Normalized scalar product approach for nearshore bathymetric estimation from X-band radar images: An assessment based on simulated and measured data," *IEEE J. Ocean. Eng.*, vol. 43, no. 1, pp. 221–237, Oct. 2017.

[11] D. A. Honegger, M. C. Haller, and R. A. Holman, "High-resolution bathymetry estimates via X-band marine radar: 1. Beaches," *Coastal Eng.*, vol. 149, pp. 39–48, Jul. 2019, doi: 10.1016/j.coastaleng.2019.03.003.

[12] P. Chernyshov, T. Vrecica, M. Streßer, R. Carrasco, and Y. Toledo, "Rapid wavelet-based bathymetry inversion method for nearshore X-band radars," *Remote Sens. Environ.*, vol. 240, Apr. 2020, Art. no. 111688. [Online]. Available: https://linkinghub.elsevier.com/retrieve/pii/S0034425720300572, doi: 10.1016/j.rse.2020.111688.

[13] C. M. Senet, J. Seemann, and F. Ziemer, "The near-surface current velocity determined from image sequences of the sea surface," *IEEE Trans. Geosci. Remote Sens.*, vol. 39, no. 3, pp. 492–505, Mar. 2001.

[14] C. M. Senet, J. Seemann, S. Flampouris, and F. Ziemer, "Determination of bathymetric and current maps by the method DiSC based on the analysis of nautical X-band radar image sequences of the sea surface (November 2007)," *IEEE Trans. Geosci. Remote Sens.*, vol. 46, no. 8, pp. 2267–2279, Aug. 2008.

[15] W. Huang, R. Carrasco, C. Shen, E. W. Gill, and J. Horstmann, "Surface current measurements using X-band marine radar with vertical polarization," *IEEE Trans. Geosci. Remote Sens.*, vol. 54, no. 5, pp. 2988–2997, May 2016.

[16] B. Lund *et al.*, "Near-surface current mapping by shipboard marine X-band radar: A validation," *J. Atmos. Ocean. Technol.*, vol. 35, no. 5, pp. 1077–1090, May 2018. [Online]. Available: https://journals.ametsoc.org/view/journals/atot/35/5/jtech-d-17-0154.1.xml

[17] B. Lund *et al.*, "Marine X-band radar currents and bathymetry: An argument for a wave number-dependent retrieval method," *J. Geophys. Res., Oceans*, vol. 125, no. 2, pp. 1–23, Feb. 2020, doi: 10.1029/2019JC015618.

[18] J. C. N. Borge, K. Hessner, and K. Reichert, "Estimation of the significant wave height with X-band nautical radars," in *Proc. 18th Int. Conf. Offshore Mech.*, 1999, pp. 1–8.

[19] H. Dankert, J. Horstmann, and W. Rosenthal, "Ocean wind fields retrieved from radar-image sequences," *J. Geophys. Res., Oceans*, vol. 108, no. 11, pp. 1–11, 2003.

[20] H. Dankert and J. Horstmann, "A marine radar wind sensor," *J. Atmos. Ocean. Technol.*, vol. 24, pp. 1629–1642, Sep. 2007, doi: 10.1175/JTECH2083.1.

[21] R. Vicen-Bueno, "Real-time ocean wind vector retrieval from marine radar image sequences acquired at grazing angle," *J. Atmos. Ocean. Technol.*, vol. 30, no. 1, pp. 127–139, Jan. 2013, doi: 10.1175/JTECH-D-12-00027.1.

[22] H. Dankert and W. Rosenthal, "Ocean surface determination from X-band radar-image sequences," *J. Geophys. Res. C, Oceans*, vol. 109, no. 4, pp. 1–11, 2004.

[23] H. Dankert, J. Horstmann, and W. Rosenthal, "Wind- and wave-field measurements using marine X-band radar-image sequences," *IEEE J. Ocean. Eng.*, vol. 30, no. 3, pp. 534–542, Jul. 2005.

[24] J. C. Nieto-Borge, G. R. Rodríguez, K. Hessner, and P. I. González, "Inversion of marine radar images for surface wave analysis," *J. Atmos. Ocean. Technol.*, vol. 21, pp. 1291–1300, Aug. 2004.

[25] S. Støle-Hentschel, J. Seemann, J. C. Nieto-Borge, and K. Trulsen, "Consistency between sea surface reconstructions from nautical X-band radar Doppler and amplitude measurements," *J. Atmos. Ocean. Technol.*, vol. 35, no. 6, pp. 1201–1220, Jun. 2018.

[26] P. Chernyshov, T. Vrecica, and Y. Toledo, "Inversion of nearshore X-band radar images to sea surface elevation maps," *Remote Sens.*, vol. 10, no. 12, p. 1919, Nov. 2018. [Online]. Available: http://www.mdpi.com/2072-4292/10/12/1919

[27] W. Navarro, J. C. Velez, A. Orfila, and S. Lonin, "A shadowing mitigation approach for sea state parameters estimation using X-band remotely sensing radar data in coastal areas," *IEEE Trans. Geosci. Remote Sens.*, vol. 57, no. 9, pp. 6292–6310, Sep. 2019.

[28] W. J. Plant, W. C. Keller, and A. Cross, "Parametric dependence of ocean wave-radar modulation transfer functions," *J. Geophys. Res., Oceans*, vol. 88, no. C14, pp. 9747–9756, Nov. 1983.

[29] J. A. McGregor, E. M. Poulter, and M. J. Smith, "S band Doppler radar measurements of bathymetry, wave energy fluxes, and dissipation across an offshore bar," *J. Geophys. Res., Oceans*, vol. 103, no. C9, pp. 779–789, 1998.

[30] P. A. Hwang and M. A. Sletten, "Energy dissipation of wind-generated waves and whitecap coverage," *J. Geophys. Res., Oceans*, vol. 113, no. 2, pp. 1–12, 2008.

[31] R. Carrasco, J. Horstmann, and J. Seemann, "Significant wave height measured by coherent X-band radar," *IEEE Trans. Geosci. Remote Sens.*, vol. 55, no. 9, pp. 5355–5365, Sep. 2017.

[32] R. Carrasco, M. Streßer, and J. Horstmann, "A simple method for retrieving significant wave height from Dopplerized X-band radar," *Ocean Sci.*, vol. 13, no. 1, pp. 95–103, Feb. 2017.

[33] A. T. Jessup, "Detection and characterization of deep water wave breaking using moderate incidence angle microwave backscatter from the sea surface," Ph.D. dissertation, Woods Hole Oceanographic Inst., Massachusetts Inst. Technol., Cambridge, MA, USA, 1990. [Online]. Available: https://hdl.handle.net/1912/3149

[34] A. T. Jessup, W. K. Melville, and W. C. Keller, "Breaking waves affecting microwave backscatter: 1. Detection and verification," *J. Geophys. Res.*, vol. 96, no. C11, p. 20547, 1991, doi: 10.1029/91jc01993.

[35] A. T. Jessup, W. K. Melville, and W. C. Keller, "Breaking waves affecting microwave backscatter: 2. Dependence on wind and wave conditions," *J. Geophys. Res.*, vol. 96, no. C11, p. 20561, 1991.

[36] S. J. Frasier, Y. Liu, and R. E. Mcintosh, "Space-time properties of radar sea spikes and their relation to wind and wave conditions," *J. Geophys. Res.*, vol. 103, no. 18, pp. 745–757, 1998.

[37] W. J. Plant, W. C. Keller, and J. W. Wright, "Modulation of coherent microwave backscatter by shoaling waves," *J. Geophys. Res., Oceans*, vol. 83, no. C3, pp. 1347–1352, 1978.

[38] B. L. Lewis and I. D. Olin, "Experimental study and theoretical model of high-resolution radar backscatter from the sea," *Radio Sci.*, vol. 15, no. 4, pp. 815–828, Jul. 1980, doi: 10.1029/rs015i004p00815.

[39] W. C. Keller, W. J. Plant, and G. R. Valenzuela, "Observation of breaking ocean waves with coherent microwave radar," in *Wave Dynamics and Radio Probing of the Ocean Surface*. Boston, MA, USA: Springer, 1986, pp. 285–293. [Online]. Available: http://link.springer.com/10.1007/978-1-4684-8980-4_20

[40] J. A. Puleo, "Comparison of optical and radar measurements of surf and swash zone velocity fields," *J. Geophys. Res.*, vol. 108, no. C3, p. 3100, 2003, doi: 10.1029/2002JC001483.

[41] G. Farquharson, S. J. Frasier, B. Raubenheimer, and S. Elgar, "Microwave radar cross sections and Doppler velocities measured in the surf zone," *J. Geophys. Res., Oceans*, vol. 110, no. C12, pp. 1–12, 2005.

[42] Y. C. Lin, C. C. Chang, M. C. Lee, H. C. Chan, and J. M. Leu, "Detection of breaking waves using X-band pulse radar in the nearshore region," *China Ocean Eng.*, vol. 27, no. 4, pp. 549–556, Aug. 2013. [Online]. Available: http://link.springer.com/10.1007/s13344-013-0046-4

[43] P. A. Catalán, M. C. Haller, and W. J. Plant, "Microwave backscattering from surf zone waves," *J. Geophys. Res., Oceans*, vol. 119, no. 5, pp. 3098–3120, May 2014, doi: 10.1002/2014jc009880.
[44] F. Bass, I. Fuks, A. Kalmykov, I. Ostrovsky, and A. Rosenberg, "Very high frequency radiowave scattering by a disturbed sea surface Part II: Scattering from an actual sea surface," *IEEE Trans. Antennas Propag.*, vol. AP-16, no. 5, pp. 560–568, Sep. 1968.
[45] J. Wright, "A new model for sea clutter," *IEEE Trans. Antennas Propag.*, vol. AP-16, no. 2, pp. 217–223, Mar. 1968.
[46] S. O. Rice, "Reflection of electromagnetic waves from slightly rough surfaces," *Commun. Pure Appl. Math.*, vol. 4, nos. 2–3, pp. 351–378, Aug. 1951.
[47] G. R. Valenzuela, "Theories for the interaction of electromagnetic and oceanic waves—A review," *Boundary-Layer Meteorol.*, vol. 13, nos. 1–4, pp. 61–85, 1978.
[48] W. Alpers, D. B. Ross, and C. L. Rufenach, "On the detectability of ocean surface waves by real and synthetic aperture radar," *J. Geophys. Res.*, vol. 86, no. C7, pp. 6481–6498, 1981.
[49] R. Romeiser, A. Schmidt, and W. Alpers, "A three-scale composite surface model for the ocean wave-radar modulation transfer function," *J. Geophys. Res.*, vol. 99, no. C5, pp. 9785–9801, 1994.
[50] G. S. Brown, "Guest editorial–special issue on low-grazing-angle backscatter from rough surfaces," *IEEE Trans. Antennas Propag.*, vol. 46, no. 1, pp. 1–2, Jan. 1998. [Online]. Available: http://ieeexplore.ieee.org/document/655445/
[51] W. J. Plant and G. Farquharson, "Wave shadowing and modulation of microwave backscatter from the ocean," *J. Geophys. Res.-Oceans*, vol. 117, no. C8, pp. 1–14, 2012.
[52] O. M. Phillips, "Radar returns from the sea surface—Bragg scattering and breaking waves," *J. Phys. Oceanogr.*, vol. 18, no. 8, pp. 1065–1074, 1988, doi: 10.1175/1520-0485(1988)018<1065:RRFTSS>2.0.CO;2.
[53] D. B. Trizna, "Statistics of low grazing angle radar sea scatter for moderate and fully developed ocean waves," *IEEE Trans. Antennas Propag.*, vol. 39, no. 12, pp. 1681–1690, Dec. 1991.
[54] P. H. Lee, "X band microwave backscattering from ocean waves," *J. Geophys. Res.*, vol. 100, no. C2, pp. 2591–2611, 1995.
[55] D. B. Trizna and D. J. Carlson, "Studies of dual polarized low grazing angle radar sea scatter in nearshore regions," *IEEE Trans. Geosci. Remote Sens.*, vol. 34, no. 3, pp. 747–757, May 1996.
[56] M. C. Haller and D. R. Lyzenga, "Comparison of radar and video observations of shallow water breaking waves," *IEEE Trans. Geosci. Remote Sens.*, vol. 41, no. 4, pp. 832–844, Apr. 2003.
[57] H. W. Melief, H. Greidanus, P. van Genderen, and P. Hoogeboom, "Analysis of sea spikes in radar sea clutter data," *IEEE Trans. Geosci. Remote Sens.*, vol. 44, no. 4, pp. 985–993, Apr. 2006.
[58] P. A. Hwang, M. A. Sletten, and J. V. Toporkov, "An empirical study of breaking wave contribution to radar backscatter from the ocean surface at low grazing angle," in *Proc. IGARSS*, 2008, pp. 113–116.
[59] P. A. Hwang, M. A. Sletten, and J. V. Toporkov, "Breaking wave contribution to low grazing angle radar backscatter from the ocean surface," *J. Geophys. Res.*, vol. 113, no. C9, pp. 1–12, 2008.
[60] M. A. Sletten and J. Wu, "Ultrawideband, polarimetric radar studies of breaking waves at low grazing angles," *Radio Sci.*, vol. 31, no. 1, pp. 181–192, Jan. 1996, doi: 10.1029/95rs01762.
[61] L. Wetzel, "On microwave scattering by breaking waves," in *Wave Dynamics and Radio Probing of the Ocean Surface*, O. M. Phillips and K. Hasselmann, Eds. Boston, MA, USA: Springer, 1986, doi: 10.1007/978-1-4684-8980-4_19.
[62] W. J. Plant, "A model for microwave Doppler sea return at high incidence angles: Bragg scattering from bound, tilted waves," *J. Geophys. Res., Oceans*, vol. 102, no. C9, pp. 21131–21146, 1997.
[63] M. J. Smith, E. M. Poulter, and J. A. McGregor, "Doppler radar measurements of wave groups and breaking waves," *J. Geophys. Res., Oceans*, vol. 101, no. C6, pp. 14269–14282, Jun. 1996.
[64] D. Miret, G. Soriano, F. Nouguier, P. Forget, M. Saillard, and C.-A. Guérin, "Sea surface microwave scattering at extreme grazing angle: Numerical investigation of the Doppler shift," *IEEE Trans. Geosci. Remote Sens.*, vol. 52, no. 11, pp. 7120–7129, Nov. 2014.
[65] J. Horstmann *et al.*, "A coherent-on-receive X-band marine radar for ocean observations," Tech. Rep., 2020.
[66] B. Baschek *et al.*, "The coastal observing system for northern and Arctic seas (COSYNA)," *Ocean Sci.*, vol. 13, no. 3, pp. 379–410, May 2017.
[67] M. Cysewski, M. Streßer, J. Bödewadt, P. Perthun, R. Carrasco, and J. Horstmann, "Single beam bathymetry transects at the west coast of sylt from Sep 22-26 2016," PANGAEA, 2019, doi: 10.1594/PANGAEA.898407.
[68] M. Derakhti, J. T. Kirby, M. L. Banner, S. T. Grilli, and J. Thomson, "A unified breaking onset criterion for surface gravity water waves in arbitrary depth," *J. Geophys. Res., Oceans*, vol. 125, no. 7, pp. 1–28, Jul. 2020.
[69] P. A. Catalán, M. C. Haller, R. A. Holman, and W. J. Plant, "Optical and microwave detection of wave breaking in the surf zone," *IEEE Trans. Geosci. Remote Sens.*, vol. 49, no. 6, pp. 1879–1893, Jun. 2011.
[70] R. J. Carini, C. C. Chickadel, A. T. Jessup, and J. Thomson, "Estimating wave energy dissipation in the surf zone using thermal infrared imagery," *J. Geophys. Res., Oceans*, vol. 120, no. 6, pp. 3937–3957, Jun. 2015.
[71] H. Díaz, P. A. Catalán, and G. W. Wilson, "Quantification of two-dimensional wave breaking dissipation in the surf zone from remote sensing data," *Remote Sens.*, vol. 10, no. 1, pp. 1–17, 2018.
[72] K. Martins, C. E. Blenkinsopp, R. Deigaard, and H. E. Power, "Energy dissipation in the inner surf zone: New insights from LiDAR-based roller geometry measurements," *J. Geophys. Res., Oceans*, vol. 123, no. 5, pp. 3386–3407, May 2018.
[73] B. G. Ruessink, G. Ramaekers, and L. C. van Rijn, "On the parameterization of the free-stream non-linear wave orbital motion in nearshore morphodynamic models," *Coastal Eng.*, vol. 65, pp. 56–63, Jul. 2012, doi: 10.1016/j.coastaleng.2012.03.006.
[74] S. Ermakov, V. Dobrokhotov, I. Sergievskaya, and I. Kapustin, "Suppression of wind ripples and microwave backscattering due to turbulence generated by breaking surface waves," *Remote Sens.*, vol. 12, no. 21, p. 3618, Nov. 2020. [Online]. Available: https://www.mdpi.com/2072-4292/12/21/3618
[75] Y. Y. Yurovsky, V. N. Kudryavtsev, B. Chapron, and S. A. Grodsky, "Modulation of Ka-band Doppler radar signals backscattered from the sea surface," *IEEE Trans. Geosci. Remote Sens.*, vol. 56, no. 5, pp. 2931–2948, May 2018. [Online]. Available: https://ieeexplore.ieee.org/document/8258988/
[76] J. Fuchs, D. Regas, T. Waseda, S. Welch, and M. P. Tulin, "Correlation of hydrodynamic features with LGA radar backscatter from breaking waves," *IEEE Trans. Geosci. Remote Sens.*, vol. 37, no. 5, pp. 2442–2460, Sep. 1999.
[77] C. A. V. Aguilera. *No Imagescnan.m V2.1 (Aug 2009)*. Accessed: Mar. 29, 2021. [Online]. Available: https://www.mathworks.com/matlabcentral/fileexchange/20516-imagescnan-m-v2-1-aug-2009
[78] Y. Altman. *Export_Fig*. Accessed: Mar. 29, 2021. [Online]. Available: https://github.com/altmany/export_fig/releases/tag/v3.14
[79] Y. H. Lee. *HCPARULA: High Contrast Parula-Like Colormap Generator*. Accessed: Mar. 29, 2021. [Online]. Available: https://www.mathworks.com/matlabcentral/fileexchange/61768-hcparula-high-contrast-parula-like-colormap-generator

Michael Streßer received the Diploma degree (Dipl.-Ing.) in civil engineering from the Leibniz University Hannover, Hanover, Germany, in 2014, and the Ph.D. degree (Dr.rer.nat.) in geosciences from the Christian-Albrechts University, Kiel, Germany, in 2020. In 2014, he was a Researcher at Coastal Research Station of the Lower Saxony Water Management, Coastal Defense and Nature Conservation Agency (NLWKN). Since 2015, he has been with the Department of Ocean Surface Dynamics,[1] Institute of Coastal Ocean Dynamics, Helmholtz-Zentrum Hereon,[2] Geesthacht, Germany. He has a strong focus on remote sensing of waves, currents, and bathymetry using marine Doppler radar and video cameras. His main research interests cover nearshore hydro- and morphodynamics, in particular their measurement and modeling.

[1]Formerly Department of Radar Hydrography.
[2]Formerly Institute of Coastal Research, Helmholtz-Zentrum Geesthacht.

Jörg Seemann received the Diploma degree in physics and the Ph.D. degree in geosciences from the University of Hamburg, Hamburg, Germany, in 1993 and 1997, respectively.

He is a Research Scientist with the Department of Ocean Surface Dynamics,[1] Institute of Coastal Ocean Dynamics, Helmholtz-Zentrum Hereon,[2] Geesthacht, Germany. His research interests include the development of signal and image processing algorithms to retrieve hydrographic parameters from incoherent and coherent radar data. He has developed a method to retrieve high-resolution current and bathymetric maps from radar backscatter intensity images and is involved in the wave measurement with Doppler radar. His scientific focus is on oceanic and coastal radar remote sensing.

Ruben Carrasco received the B.Eng. degree in industrial engineering from the Universidad de Alcalá, Madrid, Spain, in 2009.

He was with the Department of Signal Theory and Communications, Universidad de Alcalá, Alcala de Henares, Spain, working on his B.Eng. thesis related to ship detection in marine environments. From 2011 to 2014, he was a Remote Sensing Engineer with the Center for Maritime Research and Experimentation, NATO Science and Technology Organization, La Spezia, Italy. Since 2014, he has been a Research Engineer with the Department of Ocean Surface Dynamics,[1] Institute of Coastal Ocean Dynamics, Helmholtz-Zentrum Hereon,[2] Geesthacht, Germany. His research interests include artificial intelligence systems, radar signal processing, and pattern recognition.

Mr. Carrasco received in Arquimedes 2009 the Grupo Santander Award within Spain contest for young scientists.

Marius Cysewski received the Diploma degree [Dipl.-Ing. (FH)] in geomatics and hydrography and the M.Sc. degree in geomatics from the HafenCity University, Hamburg, Germany, in 2003 and 2011, respectively.

Since 2001, he has been with the Department of Ocean Surface Dynamics,[1] Institute of Coastal Ocean Dynamics, Helmholtz-Zentrum Hereon,[2] Geesthacht, Germany. He is experienced in onboard data acquisition and post-processing of hydrographic sensor data, in particular from vessel-mounted Acoustic Doppler Current Profilers (ADCPs) and marine radar. He has presented his research on many national and international science conferences and as a coauthor of scientific articles. His main project is the development of Radar Doppler Current Profiler (RDCP) and the quality assessment of current measurements in the context of retrieving geophysical parameters.

Jochen Horstmann received the Diploma degree in physical oceanography (Dipl.-Oz.) and the Ph.D. degree in earth sciences (Dr.rer.nat.) from the University of Hamburg, Hamburg, Germany, in 1997 and 2002, respectively.

He was with GKSS Research Center, Geesthacht, Germany, where he joined the Coupled Model Systems Group in 1995 and has been a Research Scientist with the Institute for Coastal Research since 2002. Since 2007, he has been an Adjunct Professor with the Rosenstiel School of Marine and Atmospheric Science, University of Miami, Coral Gables, FL, USA. In 2002, he was a Visiting Scientist with the Applied Physics Laboratory of the John Hopkins University, Laurel, MD, USA, and with the National Environmental Satellite, Data, and Information Service from NOAA, Washington, DC, USA. In 2004 and 2005, he was a Visiting Scientist with the Center for Southeastern Tropical Advanced Remote Sensing of the University of Miami. From 2008 to 2013, he was a Senior Remote Sensing Scientist with Nato Undersea Research Center, La Spezia, Italy. Since 2013, he has been the Head of the Department of Ocean Surface Dynamics, Institute of Coastal Ocean Dynamics, Helmholtz-Zentrum Hereon, Geesthacht, Germany. He has a wide experience in the field of ocean remote sensing and has published more than 80 scientific articles in international peer-reviewed journals. His main research interests are the development of applications for radar and video-based sensors with a particular focus on ocean surface and subsurface processes.

Burkard Baschek received a Diploma degree in physical oceanography from Kiel University, Kiel, Germany, in 1998, and the Ph.D. degree in earth and ocean sciences by the University of Victoria, Canada, in 2003.

After a postdoctoral scholarship and position at the Woods Hole Oceanographic Institution, he held an Assistant Professorship position in physical oceanography at the University of California at Los Angeles (UCLA), Los Angeles, CA, USA, from 2007 to 2012. Since 2012, he has been a Full Professorship at Kiel University in Sensor Development and Coastal Research. He is the Director of the Institute of Coastal Ocean Dynamics, Helmholtz-Zentrum Hereon,[2] Geesthacht, Germany. His scientific focus is on small-scale physical ocean dynamics and the interaction with biological processes. In order to observe the processes at very small temporal and spatial scales, he developed a wide range of novel instruments and sensors that are used in multiplatform experiments in the coastal ocean. His research is presented to the public using various immersive media techniques, such as virtual and augmented reality and planetariums.

Grant Deane received the M.Sc. degree from The University of Auckland, Auckland, New Zealand, in 1983, and the D.Phil. degree from the University of Oxford, Oxford, U.K., in 1989.

He is a Researcher with the Marine Physical Laboratory, Scripps Institution of Oceanography, UCSD, La Jolla, CA, USA. His work over the past 25 years focuses on breaking waves, underwater acoustics, and glacier acoustics research in the Arctic. He seeks to understand how ocean/atmosphere and ice/ocean interactions can be measured and monitored using underwater sound and what this means for gas exchange, aerosol generation, melting glaciers and sea level rise. He also earned his B.Sc. Grant from The University of Auckland and is a fellow of the Acoustical Society of America.

Dr. Deane received the A.B. Wood Medal in 1997 and the Sagar Geophysics Prize from Auckland University in 1986.